Nano Research

Open Access

Research Article

# A self-motivated carrier free nanoplatform for synergistic photodynamic and ferroptosis-based therapy for targeted antitumor treatment

Chutong Tian[1,2,3,§], Wenjing Ma[1,§], Jianbin Shi[1,§], Jia Deng[1], Zeping Gao[1], Haowen Tian[1], Ayumi Kikkawa[4], Kaho Tanaka[4], Ronggang Xi[2], Cong Luo[1,3], Xiaobo Wang[2] ✉, and Ken-ichiro Kamei[1,3,4,5,6,7] ✉

[1] *Department of Pharmaceutics, Wuya College of Innovation, Shenyang Pharmaceutical University, Shenyang 110016, China*
[2] *Pharmacy Department, the 967th Hospital of PLA Joint Logistics Support Force, Dalian 116021, China*
[3] *Joint International Research Laboratory of Intelligent Drug Delivery Systems, Ministry of Education, Shenyang 110016, China*
[4] *Graduate School and Faculty of Pharmaceutical Sciences, Kyoto University, Yoshida-Ushinomiya-cho, Sakyo-ku, Kyoto 606-8501, Japan*
[5] *Institute for Integrated Cell-Material Sciences (WPI-iCeMS), Institute for Advanced Study, Kyoto University, Yoshida-Ushinomiya-cho, Sakyo-ku, Kyoto 606-8501, Japan*
[6] *Programs of Biology and Bioengineering, Divisions of Science and Engineering, New York University Abu Dhabi, Abu Dhabi 129188, United Arab Emirates*
[7] *Department of Biomedical Engineering, Tandon School of Engineering, New York University, MetroTech, Brooklyn, NY 11201, USA*
§ *Chutong Tian, Wenjing Ma, and Jianbin Shi contributed equally to this work.*

**Cite this article:** *Nano Research*, **2025**, *18*, 94907374. https://doi.org/10.26599/NR.2025.94907374

**ABSTRACT:** Photodynamic therapy (PDT) has been extensively investigated as an alternative cancer treatment; however, its efficacy is limited by the low oxygen content and excess glutathione (GSH) in tumor tissues. With the emergence of ferroptosis, which also impacts redox homeostasis, a combined PDT-ferroptosis approach holds promise for amplifying the efficacy of both treatments. However, concerns persist regarding biocompatibility and tumor-specific release. Here, we report a self-motivated co-nanoassembly for combined PDT and ferroptosis-driven tumor therapy. We first modify linoleic acid with protoporphyrin IX to form a lipidic derivative (denoted as PLA) and develop a light-boosted carrier-free nanoplatform (PLA@R NPs) by co-assembling the ferroptosis inducer RAS-selective lethal 3 (RSL3) and PLA. Upon light irradiation, reactive oxygen species produced by PDT trigger linoleic acid peroxidation, leading to the destruction of the nanoparticles and the release of RSL3. The rapid release of RSL3 enhances PDT sensitivity by depleting GSH and utilizing the Fenton reaction to supplement oxygen. Additionally, PDT accelerates lipid peroxidation, further inducing ferroptosis. This self-motivated effect increases oxidative stress in tumor tissues, as confirmed by a tumor-on-a-chip model. Moreover, the *in vivo* therapeutic effect with the PLA@R NPs is significant, demonstrating the promising potential of combining PDT and ferroptosis using a light-boosted and self-motivated nanoplatform.

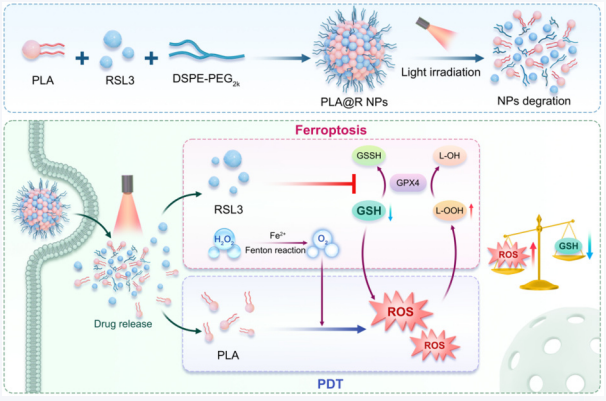


**KEYWORDS:** ferroptosis, photodynamic therapy, carrier-free nanoparticle, cancer treatment

## 1 Introduction

Photodynamic therapy (PDT) has gained increasing attention over the past few decades as a noninvasive cancer treatment, demonstrating superior advantages over traditional therapies such as chemotherapy and surgery [1, 2]. Once delivered to tumor sites, photosensitizers produce reactive oxygen species (ROS) upon light irradiation, inducing damage to cellular membranes, DNA and proteins [3, 4]. However, the efficacy of PDT is often hindered by the limited oxygen supply within hypoxic tumor microenvironments [5, 6]. In addition, tumor cells can overexpress glutathione (GSH) to neutralize ROS, further compromising the

**Received:** December 24, 2024; **Revised:** March 14, 2025
**Accepted:** March 14, 2025

✉Address correspondence to Ken-ichiro Kamei, kk4801@nyu.edu; Xiaobo Wang, wxbbenson0653@sina.com

effectiveness of PDT [7, 8]. Consequently, PDT alone may not be sufficient to completely eradicate primary tumors. Therefore, it is critical to develop sensitization strategies that enhance the effectiveness of PDT through synergistic combinations.

One promising approach to overcome these limitations involves combining PDT with ferroptosis, a unique type of programmed cell death. Unlike other forms of cell death, ferroptosis is characterized by the defects in lipid peroxide (LPO) repair, typically caused by the inhibition of glutathione peroxidase 4 (GPX4) [9–11]. RAS-selective lethal 3 (RSL3) is a well-known ferroptosis inducer that targets GPX4. However, high levels of RSL3 are required to trigger ferroptosis *in vivo*, which can lead to severe dose-related toxicity [12, 13]. Moreover, the poor pharmacokinetic properties of RSL3 limit its potential clinical applications [14, 15]. Given the limitations of PDT and ferroptosis, and their shared involvement in redox homeostasis, we hypothesize that combining these approaches could significantly amplify oxidative stress, leading to more effective tumor cell elimination. PDT can promote ferroptosis through robust ROS generation [16], while inactivating GPX4 disrupts the GSH-related oxidation defense system in tumor cells, thereby enhancing PDT efficiency [17]. Furthermore, ferroptosis-associated Fenton reactions ($(Fe^{2+} + H_2O_2 \rightarrow Fe^{3+} + OH^- + \cdot OH$, $2Fe^{3+} + H_2O_2 \rightarrow 2Fe^{2+} + O_2 + 2H^+$) have been reported to alleviate tumor hypoxia [18]. Thus, PDT and ferroptosis can work synergistically to achieve a more potent anti-tumor effect. However, the targeted delivery of photosensitizers and ferroptosis inducers to tumor regions remains challenging.

Many photosensitizers and classical ferroptosis inducers, such as RSL3, face challenges due to their poor solubility in aqueous environments and suboptimal pharmacokinetics, which result in limited accumulation in tumor sites [15, 19, 20]. Moreover, ensuring that both drugs reach the target site simultaneously during combined administration is difficult and can lead to overlapping toxicity. To address these challenges, recent efforts have focused on using nanocarriers—such as proteins, polymers and inorganic materials—to enhance drug solubility and improve circulation stability. These advances have led to the development of emerging nanoplatforms designed for synergistic ferroptosis and PDT cancer therapy [21, 22]. Despite these advancements, concerns remain about unsatisfactory drug loading rates, potential carrier-related toxicity and non-specific drug leakage. Therefore, novel strategies that offer more effective drug loading capacities and greater specificity in responsive property are urgently needed for the combined therapy of PDT and ferroptosis.

To overcome these limitations, a promising alternative is the development of carrier-free nano delivery systems. These systems allow for the self or co-assembly of drugs without the assistance of excipients, offering high drug-loading capacity and minimal nanocarrier-associated toxicity [23, 24]. However, not all drugs naturally possess the ability to self-assemble, and achieving tumor-specific drug release from pure drug nanoassemblies remains challenging. Fortunately, lipid modification has emerged as an effective strategy to endow certain drugs with self-assembly capabilities [25, 26]. For instance, fatty acids have been shown to act as effective assembly modules [27]. Among these, polyunsaturated fatty acids (PUFAs) like linoleic acid, are particularly appealing because they serve as substrates for lipid peroxidation (LPO) chain reactions and are highly susceptible to ROS [28]. This suggests that employing PUFAs as modification modules could further propagate ferroptosis, while also functioning as release switches that respond to ROS generated by PDT, as their assembly capacity diminishes during lipid peroxidation.

Here we report a self-motivated co-nanoassembly for combined PDT and ferroptosis-driven tumor therapy (Fig. 1). We develop a lipidic derivative (denoted as PLA) of photosensitizer protoporphyrin IX (PpIX) through linoleic acids (LA) modification. A self-motivated nanoplatform (PLA@R NPs) is then constructed using a drug-delivery-drug (DDD) engineering strategy. Upon light irradiation, the PpIX-induced ROS oxidates LA, leading to nanoparticle distruption and subsequent RSL3 release. As a result, PDT and RSL3-triggered ferroptosis synergistically inhibit tumor growth in traditional cell models, dynamic tumor-on-a-chip (TOC) models and *in vivo* animal models without significant toxicity, offering a promising strategy for safe and effective tumor therapy.

## 2 Results and discussion

### 2.1 Synthesis of PLA and preparation of PLA@R NPs

To endow the drug with assembly capacity and achieve light-controlled drug release, we modified LAs into the photosensitizer PpIX to form a lipidic derivative PLA (Fig. S1 in the Electronic Supplementary Material (ESM)). The structure was confirmed using $^1$H-NMR and mass spectrum (Figs. S2 and S3 in the ESM). The nanoplatform was fabricated via the co-precipitation nanotechnology, with 20% (w/w) amphiphilic 1,2-distearoyl-sn-glycero-3-phosphoethanolamine-N-[methoxy(polyethylene glycol)-2000] (DSPE-$PEG_{2K}$) was used to improve the stability and pharmacokinetics of the nanoplatform (Fig. 2(a)). We found that PLA was also able to self-assemble into uniform NPs with size of around 120 nm (Table S1 in the ESM). To determine the optimal co-assmebly ratio of PLA and RSL3, we screened a series of ratios (3:1 to 1:3) of the drug pair by measuring particle size and polydispersity index (PDI). As the results, the combination of RSL3 and PLA could efficiently co-assemble into uniform NPs at a wide ratio and achieve the optimal size with low PDI (< 0.2) at a ratio of 1:2 (Figs. 2(b) and 2(c)). The following studies were carried out in basis of PLA@R NPs fabricated at this ratio.

As shown in Fig. 2(d) and Table S1 in the ESM, PLA@R NPs exhibited a hydrodynamic diameter of 142.23 ± 3.44 nm with negative Zeta potential of −30.63 ± 0.12 mV, which may confer the PLA@R NPs with suitable passive targeting ability towards tumors. Transmission electron microscopy (TEM) image revealed that the PLA@R NPs exhibited a uniform spherical morphology. A significant Tyndall effect was also observed, indicating the colloidal nature of the formulation (Fig. 2(d)). Additionally, the drug loading was also calculated to be 32.24% for PpIX and 12.63% for RSL3, respectively. PLA@R NPs also demonstrated favorable colloidal stability; as shown in Fig. S4 in the ESM, no significant changes in particle size was observed after nearly one month of storage at 4 °C. Besides, PLA@R NPs also showed good colloidal stability in phosphate-buffered saline (PBS) (pH 7.4) containing 10% (v/v) fetal bovine serum (FBS) (Fig. S5 in the ESM). These results demonstrated that good colloidal stability of PLA@R NPs would certainly be in favor of the *in vivo* performance.

We then investigated the assembly mechanism of the nanoplatform. Molecular dynamics (MD) simulations were conducted to scrutinize the self-assembly mechanisms of PLA@R NPs. As shown in Fig. 2(e), hydrophobic interaction was found to be the main driving force involved in the co-assembly of PLA and

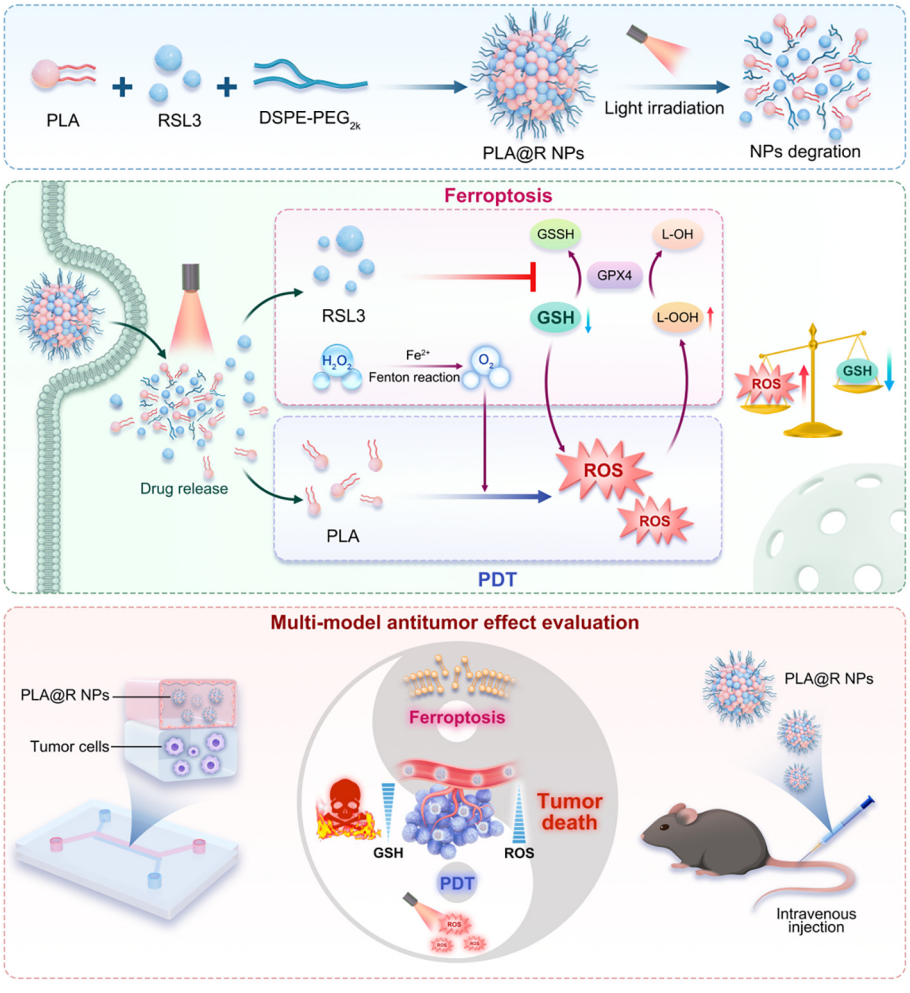


**Figure 1** Schematic diagram of the mechanisms of PLA@R NPs for tumor elimination. LA-modified photosensitizer PLA was able to readily co-assemble with RSL3 into stable nanostructure. Under light irradiation, the PpIX-induced ROS oxidates LA to destruct the nanoparticles, subsequently boosting RSL3 cascade release. When PLA@R NPs were endocytosed into tumor cells, they could rapidly disintegrate with light irradiation and release PLA and RSL3 to synergistically induce tumor PDT/ferroptosis, amplifying the tumor oxidative stress.

RSL3. Moreover, sodium dodecyl sulfate (SDS), sodium chloride (NaCl) and urea were utilized to destroy the nanoassembly by destructing hydrophobic force, electrostatic interaction and hydrogen bond, respectively. The nanoassembly stability was investigated after incubation with these salt solutions. As shown in Fig. 2(f), NaCl and urea showed little impact on the particle size of the NPs. In contrast, the particle size of the PLA@R NPs increased significantly after incubation with SDS, further confirming that hydrophobic forces dominate the nanoassembly of PLA and RSL3.

## 2.2 PLA@R NPs show light-boosted drug release characteristic

Selective RSL3 release in tumor sites is of great importance for safe drug delivery of the PLA@R NPs *in vivo*. To investigate the light-boosted drug release characteristics of the NPs, RSL3 release profiles were evaluated under both light irradiation and dark condition. As shown in Fig. 2(g), it showed limited release of RSL3 in the dark (approximately 40% after 48 h of incubation). In contrast, RSL3 release was significantly boosted, to approximately 70% at 1 h, upon light exposure. In addition, as shown in the TEM image, PLA@R NPs rapidly dissociated into smaller particles upon exposure to light irradiation (Fig. S6 in the ESM). These results suggest that the ROS, produced by the PpIX during the PDT process under 660-nm light irradiation, is capable of oxidating the LAs in the PLA structures, resulting in the rapid degradation of NPs and boosted RSL3 release (Fig. 2(h)). The light-boosted drug release patterns of the PLA@R NPs will certainly benefit potent cytotoxicity against tumor cells through rapidly triggering drug release within tumor cells, while ensuring safety to normal tissues.

## 2.3 PLA@R NPs exhibit synergistic cytotoxicity effect *in vitro*

The *in vitro* synergistic therapeutic anticancer effects of the PLA@R NPs were then verified in traditional cancer cell model through 3-(4,5-dimethylthiazol-2-yl)-2,5-diphenyltetrazolium bromide (MTT) assay under light and dark situations on two lung cancer cell lines, including human A549 cells and mouse Lewis lung cancer (LLC) cells. As shown in Fig. 2(i) and Fig. S7 in the ESM, there is no obvious therapeutic effect observed in the PLA NPs or PLA@R NPs groups without light treatment, which is consistent with the *in vitro* drug release results. The mix solution of PpIX and RSL3 showed increased cytotoxicity compared with the NPs groups in dark condition, further verifying the light-triggered characteristic of the PDT-ferroptosis co-nanoassemblies. With light irradiation, mix

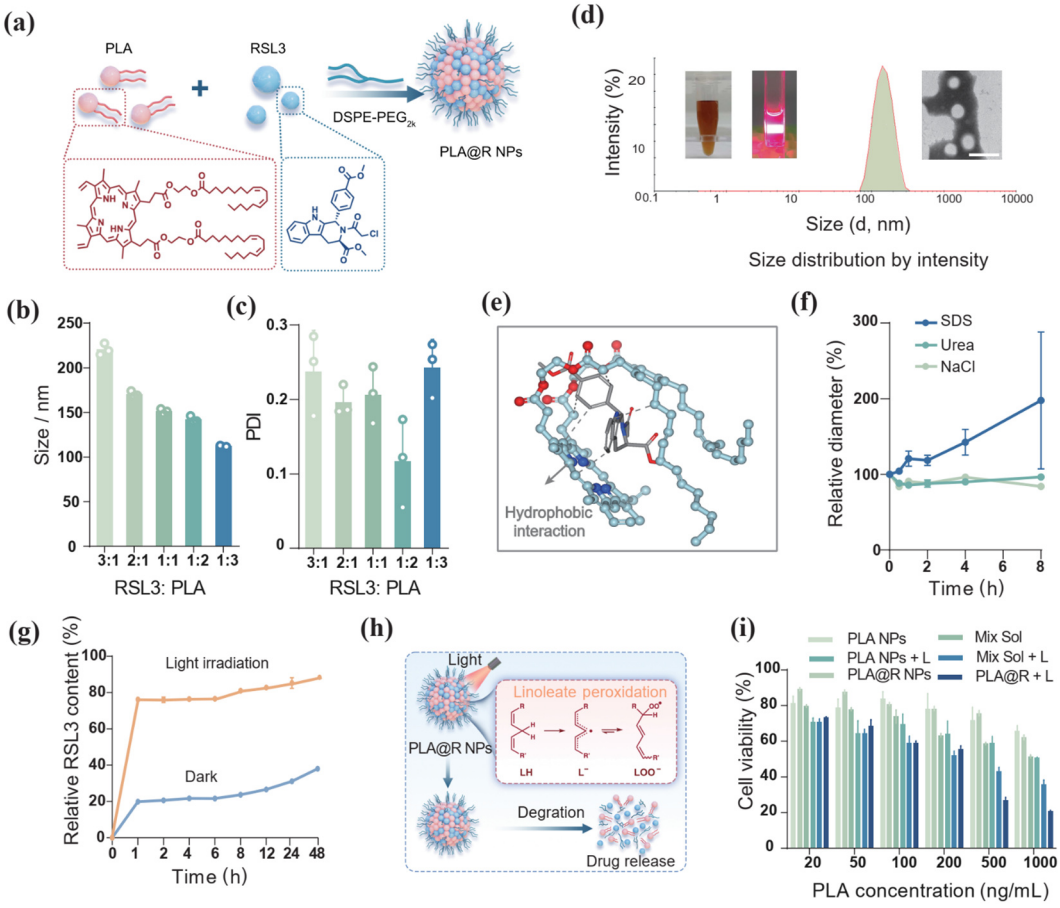


**Figure 2** Preparation and characterization of PLA@R NPs. (a) Chemical structures of PLA and RSL3 and co-assembly process of PLA@R NPs. (b) Average size and (c) PDI of co-assembled NPs at different weight ratio. (d) Size distribution, appearance and TEM image of PLA@R NPs (scale bar represents 200 nm). (e) Molecular conformation of PLA@R NPs during MD simulations. Blue structure represents PLA and gray structure represents RSL3. (f) Changes in particle size of PLA@R NPs treated with NaCl (10 mM), SDS (10 mM) and urea (10 mM). (g) Drug release profiles of PLA@R NPs under light and dark condition. (h) light-boosted drug release mechanisms of PLA@R NPs. (i) *In vitro* cytotoxicity against A549 cells treated with various formulations after 48 h. Data are portrayed as the mean value ± standard deviation ($n = 3$).

solution exhibited more remarkable concentration-dependent cytotoxicity against A549 cells than PLA NPs, implying that the combination of ferroptosis and PDT is efficient in eliminating cancer cells. We hence did not compare PLA NPs in the following experiments. PLA@R NPs also showed the best anti-cancer efficiency among all the formulations under light irradiation, which could be due to the more efficient drug delivery to cancer cells, leading to the synchronous activation of ferroptosis and PDT.

### 2.4 PLA@R NPs regulate tumor redox microenvironment *in vitro*

The microfluidic TOC platform offers significant advantages over conventional 2D and even 3D cell cultures in nanodrug delivery research. It provides a better understanding of how fluidic flows and tumor microenvironment (TME) affect nanodrug behavior [29]. To date, most *in vitro* NP cell evaluation models are based on 2D monocultures, where cells are statically incubated in media containing a constant concentration of NPs [30]. However, these platforms fail to replicate the key characteristics of the TME, such as tumor interstitial fluid, which plays a crucial role in NP uptake and accumulation within tumors [31].

To better mimic the TME, we utilize the TOC platform to compare the cellular uptake of nanoassemblies under both static and dynamic conditions, with and without a liquid flow. The TOC used was designed and fabricated (Figs. 3(a)–3(c)) [32] and the perfusion flow rate was chosen as 10 μL/min, resulting in a shear force of $2.38 \times 10^{-2}$ dyn/cm$^2$. Cellular uptake of the PLA@R NPs in A549 cells was observed using the PpIX fluorescence. Confocal imaging indicated that the fluorescence intensity of PpIX became stronger in a time-dependent manner in both NPs and solution groups under dynamic and static conditions (Fig. 3(d), and Fig. S8 in the ESM). The red intracellular fluorescence of PLA@R NPs treated cells was much stronger than that of mix solution-treated cells, which proved the better cellular internalization ability of NPs over free drugs. Additionally, compared with the static incubation, intracellular fluorescence intensity was significantly decreased under dynamic conditions, suggesting that the fluidic shear stress decreased cellular drug uptake (Fig. 3(e)).

The cellular production of ROS was initially assessed using the DCFH-DA probe under different treatments in the TOC. Minimal green fluorescence was observed under dark conditions, while PLA@R NPs group was found to produce 1.19-fold of ROS compared to the mix solution under light irradiation (Fig. 3(f) and Fig. S9 in the ESM). The ROS scavenger vitamin C (VC) effectively alleviated the increase in intracellular ROS levels caused by PLA@R NPs. We further used the fluorescent probe C11-BODIPY to

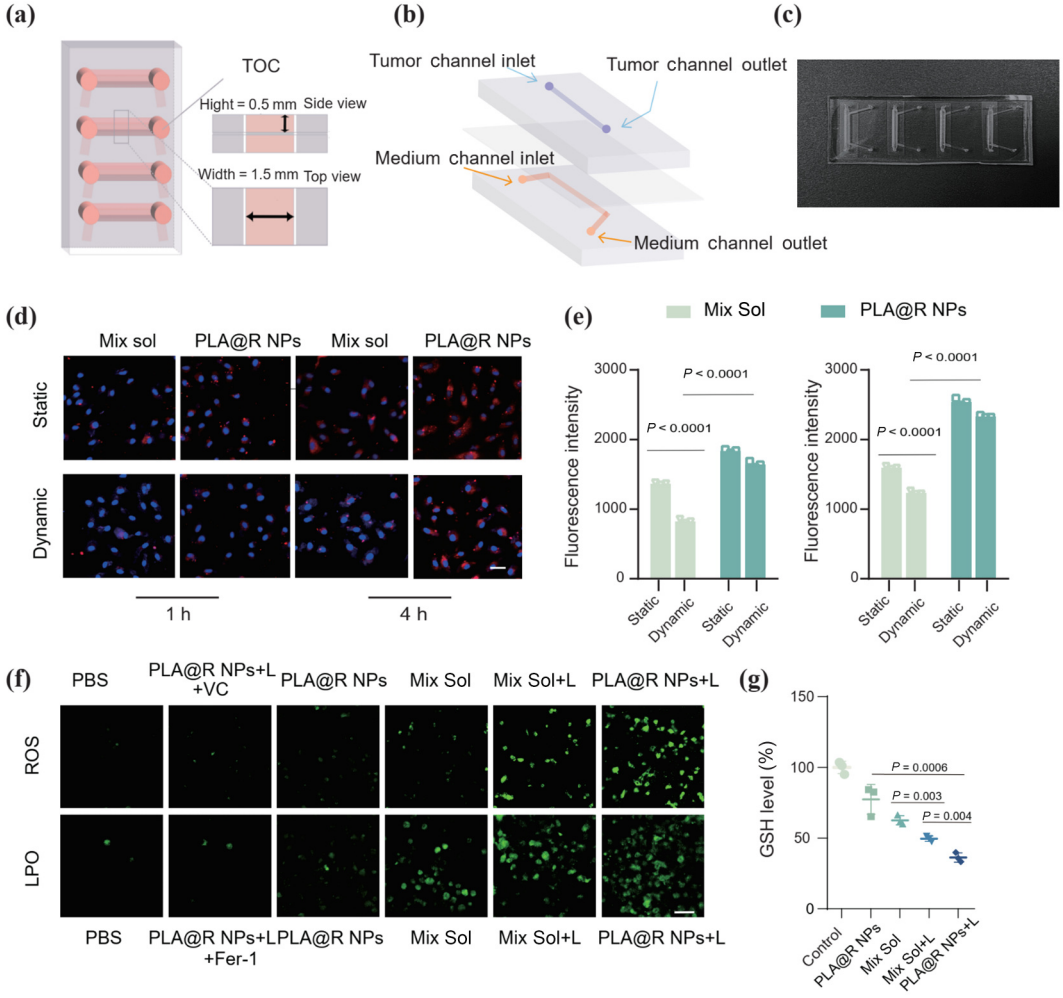


**Figure 3** Tumor redox microenvironment imbalance induced by PLA@R NPs in TOC. (a) Design overview of the TOC. (b) Schematic diagram of the TOC. The upper channels were set as tumor channel, while the lower channels were perfused with blank medium. (c) Image of the microfluidic TOC platform. (d) The CLSM images of cellular uptake of formulations in A549 cells under static or dynamic conditions at 1 h (left) and 4 h (right). Nucleus was visualized with Hoechst 33342 (10 μg/mL). Scale bar represents 50 μm. (e) Quantitative analysis of cellular uptake under static or dynamic conditions at 1 or 4 h. (f) Intracellular ROS and LPO level of cells post administration. Scale bar represents 100 μm. (g) Intracellular GSH levels in cells after treatments. Data represent a mean ± standard deviation ($n = 3$).

evaluate lipid peroxidation, a key indicator of cell ferroptosis, under different treatments. After light irradiation, LPO increased significantly in both the mix solution (1.29-fold) and NP groups (2.52-fold) compared to the non-irradiated group. The NPs group showed negligible green fluorescence under dark conditions, likely due to the limited RSL3 release. Notably, compared with the mix solution +L group, the PLA@R NPs +L group exhibited a higher level of LPO, consistent with the ROS generation trend. The LPO was attenuated by ferrostatin-1 (Fer-1), further suggesting that PLA@R NPs treatment induced ferroptosis.

In addition, we measured GSH levels under dynamic administration of different formulations (Fig. 3(g)). Cellular GSH levels decreased by 22.6% and 37.4% after treatment with PLA@R NPs and mix solution, respectively, compared to the control group. Upon light irradiation, the GSH level of mix solution and PLA@R NPs group further decreased by 50.4% and 63.7% compared to the control group. The *in vitro* GSH depletion assay confirmed PDT-induced ROS effectively consumed GSH (Fig. S10 in the ESM). These findings suggest that the observed increase in ROS and LPO, along with the reduction in GSH levels, collectively indicate a synergistic induction of ferroptosis and PDT. Moreover, PLA@R NPs demonstrate a stronger synergistic effect compared to the mix solution, likely due to their more efficient internalization into tumor cells. Light irradiation plays a crucial role as a trigger for PLA@R NPs, initiating the synergistic effect, with LA serving as the control module. Furthermore, the depletion of GSH and the oxidative damage induced by ferroptosis enhance the therapeutic efficacy of PDT, while the integration of PDT reciprocally accelerates the onset of ferroptosis. Overall, PLA@R NPs effectively regulate the redox balance within tumor cells, disrupting cellular homeostasis and consequently amplifying the therapeutic efficacy of both PDT and ferroptosis.

### 2.5 PLA@R NPs inhibit tumor cell proliferation in vascularized TOC model

Previous studies have indicated that the vascular changes associated with cancer, including tumor-induced remodeling of blood vessels, can compromise the integrity of vessel barriers [33]. Understanding these vascular changes and their impact on NPs delivery is critical for improving therapeutic strategies. TOC models are particularly effective for studying these processes because they can accurately replicate the complex interactions between tumor cells and the

surrounding vasculature under dynamic conditions that closely mimic *in vivo* environments. This allows for a more precise evaluation of how NPs interact with tumor-associated vasculature and penetrate the tumor microenvironment [34].

To further recapitulate tumor vasculature and study vascular permeability of NPs, we developed a vascularized TOC (VTOC) by integrating both a tumor vasculature structure and a tumor cell compartment within a single microfluidic platform. This design provides a more realistic and controlled microenvironment for studying NPs behavior. The top microchannel is used to model the tumor vasculature by culturing human umbilical vein endothelial cells (HUVECs), while the bottom microchannel allows for the introduction of A549 tumor cells (Fig. 4(a)). This dual-channel design enables the simultaneous study of vascular function and tumor cell responses, offering a comprehensive platform to explore how vascular permeability affects NPs delivery in the tumor context.

By using the VTOC platform, we observed that ZO-1 expression in endothelial cell borders became weak and discontinuous in the vascularized TOC compared to a control chip with vascular cells alone (Fig. 4(b) and Fig. S11 in the ESM). This reduced ZO-1 expression is consistent with the formation of leaky tumor vasculature, a hallmark of tumor tissues that facilitates increased NPs permeability.

To investigate further, we examined the vascular permeability of PLA@R NPs and mix solution within the VTOC. As shown in Fig. 4(c), PLA@R NPs exhibited faster and more efficient transendothelial transport compared to the mix solution. This enhanced permeability is likely due to the weakened barrier function of the leaky tumor vasculature, which allows for more efficient NPs delivery into the TME.

Next, we evaluated antitumor efficiency in the VTOC by measuring proliferation of A549 cells using Ki67 immunofluorescence and enzyme-linked immunosorbent assay (ELISA) (Figs. 4(d) and 4(e)). Consistent with above results, tumor proliferation was only moderately inhibited when treated with the formulations under dark conditions. Irradiation could significantly slow down the tumor proliferation rate with treatment of mix solution and PLA@R NPs. Moreover, a more significant tumor growth inhibition was achieved in the PLA@R NPs +L group than mix solution +L group, as the mean tumor proliferation rates of NPs groups (167.4%) and solution groups (478.6%) after 72-h treatment. This effect is likely due to the efficient synchronous co-delivery of drugs, laser-activated drug release, and the mutual enhancement of therapeutic effects between ferroptosis and PDT.

### 2.6 PLA@R NPs increase drug blood circulation time and tumor accumulation

The *in vivo* drug delivery efficiency of nanomedicines significantly impacts therapeutic outcomes, particularly in terms of the systemic circulation time and tumor-specific accumulation. The favorable nano-size and PEGylated decoration would benefit the blood circulation time of drugs. To investigate pharmacokinetic behaviors, we administered PLA@R NPs and a mix solution to Sprague Dawley rats and quantitatively measured PpIX fluorescence in plasma at various time points after intravenous injection. As shown in Fig. 5(a), the mix solution was rapidly cleared from the blood within 2 h. In contrast, PLA@R NPs

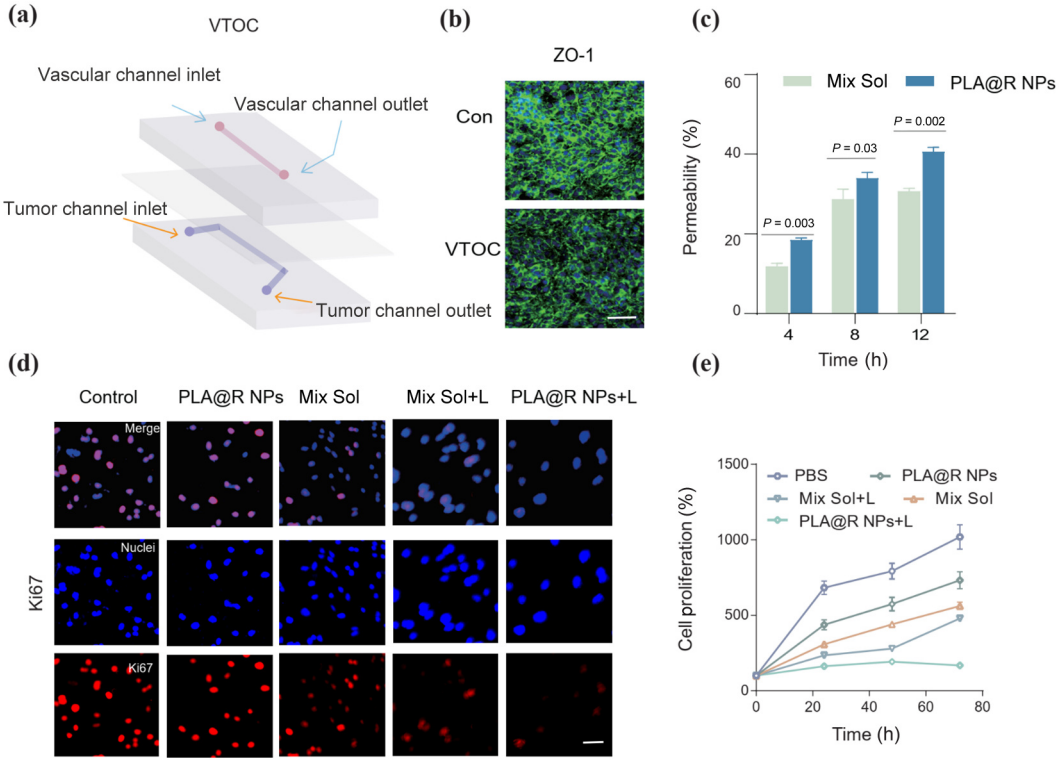


**Figure 4** Enhanced vessel permeability and tumor cell proliferation inhibition effect of PLA@R NPs in VTOC model. (a) Illustration of VTOC with the top microchannel culturing HUVECs and the bottom microchannel culturing A549 tumor cells. (b) Immunofluorescence of ZO-1of HUVECs in single vascular chip and VTOC. Scale bar represents 50 μm. (c) Vessel permeability of the formulations at 4, 8 and 12 h. (d) Immunofluorescence micrographs of Ki67 of after 36 h treatment of the formulations in VTOC. (e) Intracellular levels of Ki67 protein expression after treatment of the formulations in VTOC. Scale bar represents 50 μm. Data are portrayed as the mean ± standard deviation ($n$ = 3).

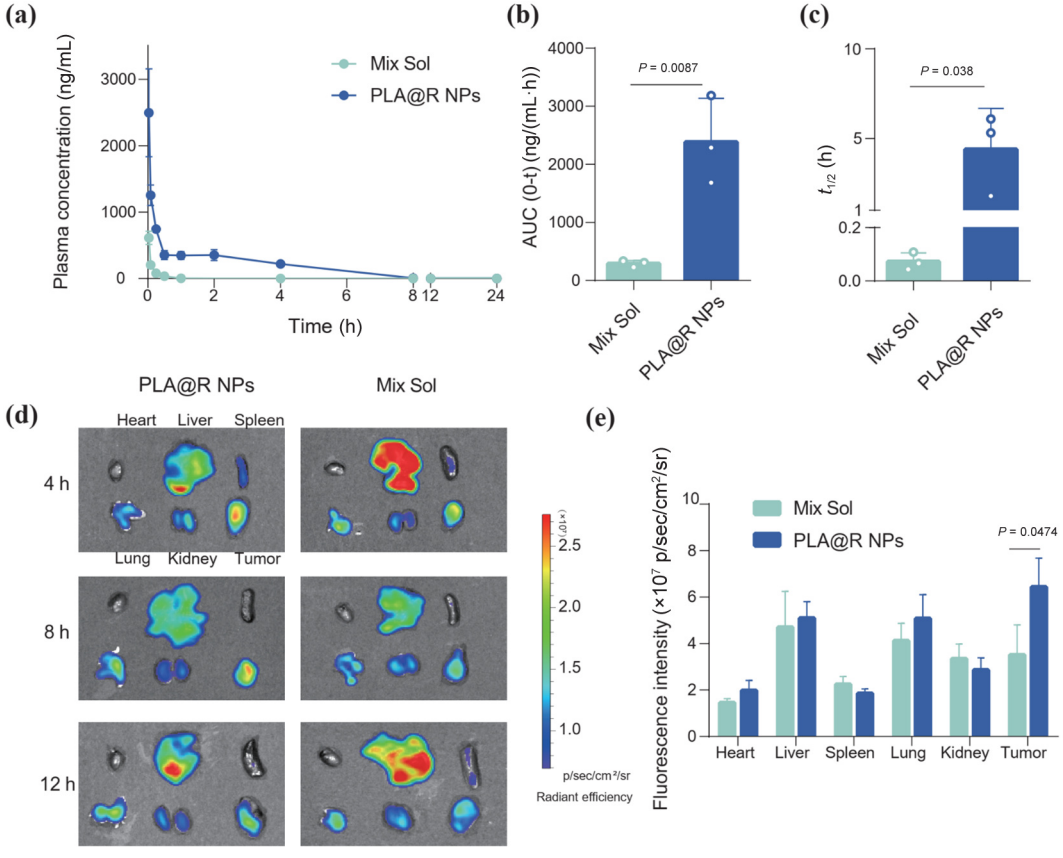


**Figure 5** *In vivo* delivery performances of PLA@R NPs. (a) Plasma concentration-time curves of PpIx in rats after intravenous injection of PLA@R NPs or Mix sol. (b) $AUC_{(0-24)}$ of formulations calculated from plasma concentration-time profiles. (C) $t_{1/2}$ of formulations calculated from plasma concentration-time profiles. (d) *Ex vivo* fluorescence images of tumor and major organs collected at 4, 8 and 12 h after intravenous injection of PLA@R NPs or Mix sol. (e) Quantitative results of the average fluorescence intensity of tumor and major organs at 8 h. Data are portrayed as the mean value ± standard deviation ($n$ = 3).

exhibited a significantly longer circulation time and a higher area under the concentration–time curve (AUC) (8.2-fold) compared to the mix solution at an equivalent PpIX dosage (Figs. 5(b) and 5(c)). These enhanced pharmacokinetic properties of PLA@R NPs are expected to improve tumor-targeting accumulation of the drug.

To further assess the *in vivo* tumor-targeting ability and biodistribution of PLA@R NPs, we conducted studies using LLC xenograft mice. Following a single injection of NPs or the mix solution, we extracted major organs and tumors for *ex vivo* imaging. As shown in Fig. 5(d), mix solution exhibited a rapid and pronounced distribution to the liver in 4 h. In contrast, the PpIX signals in tumors of PLA@R NPs group were significantly stronger than that of mix solution group, reaching a peak fluorescence intensity at 8 h. Tumor fluorescence signal nearly disappeared after 12 h treatment of the mix solution, while it still exhibited a moderate enrichment of drugs in tumor in PLA@R NPs treated-group. The consistent *ex vivo* fluorescence imaging and semi-quantitative analysis (Fig. 5(e)) results proved that the developed PLA@R NPs have enhanced targeted delivery ability and increased accumulation at tumor sites compared to the free drug, which could be attributed to their prolonged circulation time and the enhanced permeability and retention (EPR) effect.

### 2.7 PLA@R NPs exhibit enhanced antitumor effect and improved safety *in vivo*

PLA@R NPs, with favorable drug delivery properties, show great promise as anticancer nanotherapeutics. The combination of RSL3 and PLA demonstrated a synergistic effect of PDT and ferroptosis *in vitro*, with laser activation as precise switch for drug release. To evaluate the *in vivo* antitumor effects of these nanoassemblies, we conducted studies on LLC tumor-bearing mice, following the protocol outlined in Fig. 6(a). Light irradiation (660 nm, 100 mW/cm²) for 2 min to activate PDT 8-h after administration.

As shown in Figs. 6(b)–6(e), after 10 days of treatment, the tumor volumes in the PBS group increased rapidly to nearly 1000 mm³, while growth slowed to varying degrees in other groups. As expected, the mix solution and PLA NPs +L exhibited moderate antitumor effect, attributed to ferroptosis or PDT. Notably, PLA@R NPs without light irradiation also showed enhanced antitumor activity compared with the mix solution, likely due to delayed elimination and increased tumor accumulation. The mix solution +L exerted stronger proliferation than monotherapy groups (PLA NPs +L or mix solution), suggesting the synergistic effect of two drugs. In contrast, PLA@R NPs +L displayed distinct therapeutic advantages over other formulations, with potent inhibitory effects on tumor growth. This superior inhibitory effect of PLA@R NPs +L group was produced by the long blood circulation, high tumor accumulation, on-target drug release and synergistic interaction of PDT and ferroptosis. To further verify the ability of the PLA@R NPs to overcome tumor hypoxia, we performed hypoxia-inducible factor-1$\alpha$ (HIF-1$\alpha$) immunofluorescence staining on tumor tissues harvested after therapy. As shown in Fig. S12 in the ESM, HIF-1$\alpha$ fluorescence intensity in the PLA NPs +L group significantly increased compared to untreated controls, consistent with

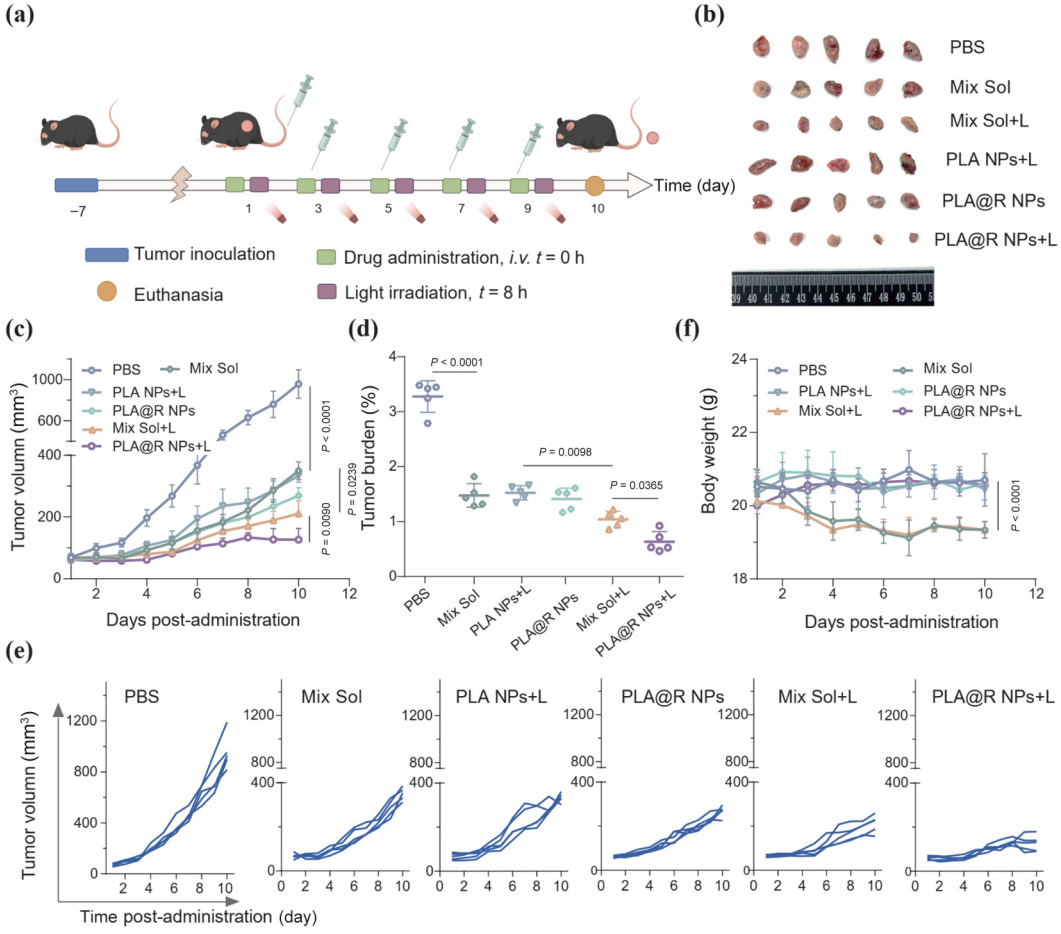


**Figure 6** Antitumor performance of PLA@R NPs *in vivo*. (a) Protocol of pharmacodynamics study. (b) Images of dissected tumors at the end of treatment. (c) Tumor volume curves during the treatment. (d) Tumor burdens at the end of treatment. (e) Individual tumor growth curves of the mice during the treatment period. (f) Body weight curves during the treatment. Data are portrayed as the mean value ± standard deviation ($n$ = 5).

exacerbated hypoxia due to oxygen consumption during PDT. In contrast, PLA@R NPs-treated groups presented significantly decreased fluorescence intensity, which is attributed to the intracellular $O_2$ generation. This alleviation of tumor hypoxia in PLA@R NPs-treated tumors arises from ferroptosis-associated Fenton-reactions. Consequently, the tumor microenvironment transitions to a normoxic state, enabling sustained ROS production during PDT and amplifying therapeutic outcomes.

Moreover, the mice treated with the mix solution (with or without light) experienced a decrease in body weight, likely due to the non-specific toxicity of RSL3. In contrast, there was no significant change in body weight and hepatorenal function parameters in NPs groups, indicating the safety of PLA@R NPs (Fig. 6(f) and Fig. S13 in the ESM). Collectively, these findings demonstrate that the utilization of PLA@R NPs effectively facilitates a synergistic effect between PDT and ferroptosis, resulting in a significantly enhanced tumoricidal effect while minimizing adverse reactions.

## 3 Conclusions

In this study, we developed a self-sensitizing nanoplatform (PLA@R NPs) that leverages the LPO chain reaction of LA to trigger ferroptosis and PDT upon light activation. The co-delivery of PpIX and RSL3 via self-assembled nanoparticles significantly enhanced ROS production and LPO, while effectively depleting GSH levels compared to the free drug mixture. We validated the therapeutic efficacy of the PLA@R NPs across various models, including a TOC, and observed that the NPs achieved successful tumor inhibition with minimal harm to healthy tissue. This antitumor effect can be attributed to several key advantages of the PLA@R NPs: high drug co-loading capacity, robust stability, efficient cellular uptake, light-triggered on-demand drug release, prolonged blood circulation, and enhanced tumor-specific accumulation. Additionally, the synergetic amplification of ferroptosis and PDT within tumors further contributes to their therapeutic potential. Overall, the PLA@R NPs represent a promising approach for nanomedicine in clinical cancer treatment, offering a potent and precise therapeutic strategy by integrating multiple mechanisms to enhance efficacy while minimizing adverse effects.

## 4 Experimental

### 4.1 Materials

Protoporphyrin IX (PpIX) was purchased from Shanghai Xianhui Pharmaceutical Co., Ltd. (Shanghai, China). Linoleic acid was purchased from Shanghai Bide Pharmatech Ltd. (Shanghai, China). RSL3 was purchased from Shanghai Bide Pharmaceutical Co., Ltd. (Shanghai, China). FBS, Dulbecco's modified Eagle medium

(DMEM), PBS, trypsin, antibiotics, MTT, Hoechst 33342, enhanced chemiluminescence (ECL) and the others were purchased from Dalian Meilunbio. Ki67 monoclonal antibody was purchased from ABclonal Technology. Ki67 ELISA Kit was purchased from Shanghai MLBio (Cat. #ml063710V).

### 4.2 Synthesis of PLA

The synthesis approach of PLA was summarized in Fig. S1 in the ESM, and its chemical structure was confirmed by high resolution mass spectra and $^1$H NMR. Linoleic acid (560 mg, 2 mmol), ethylene glycol (120 mg, 5 mmol), 4-Dimethylaminopyridine (DMAP) (24.6 mg, 0.2 mmol) and 1-Ethyl-3-(3-dimethylaminopropyl) carbodiimide hydrochloride (EDCI) (110 mg, 1.2 mmol) were dissolved in dry $CH_2Cl_2$ (50 mL) and stirred at 25 °C for 12 h. The reaction mixture was concentrated under reduced pressure. Silica gel chromatography (10:1 to 2:1 n-hexane/ethyl acetate) was used to give the pure intermediate compound. A mixture of PpIX (1126 mg, 1 mmol), DMAP (24.6 mg, 0.2 mmol), EDCI (110 mg, 1.2 mmol) and intermediate compound (972 mg, 3 mmol) in dry $CH_2Cl_2$ (50 mL) were stirred at 25 °C for 48 h. The reaction mixture was concentrated under reduced pressure. Silica gel chromatography (20:1 to 1.5:1 n-hexane/ethyl acetate) was used to give the pure PLA.

### 4.3 Preparation and characterization of PLA@R NPs

The PLA@R NPs were fabricated via one-step nanoprecipitation method. Specifically, PLA and RSL3 were dissolved in tetrahydrofuran at a concentration of 1 mg/mL. Then, a mixture of PLA and RSL3 at weight ratios of 1:3, 1:2, 1:1, 2:1 or 3:1 was dropwise added into deionized water (2 mL) without or with DSPE-$PEG_{2K}$ under stirring (1300 rpm) for 2 min to prepare non-PEGylated or PEGylated PLA@R NPs. Tetrahydrofuran in the dispersion was removed by vacuum rotary evaporation at 35 °C. PLA NPs was prepared by a similar preparation only with PLA. Then, the stability of NPs was evaluated in PBS (pH 7.4) consisting of 10% FBS in constant temperature shake (37 °C). Furthermore, the ZetaSizer (NanoZS, Malvern Panalytical, UK) was used to characterize the particle sizes, PDI and Zeta potentials of NPs. Morphological observations of the PLA@R NPs were conducted by staining the samples with a 2% phosphotungstic acid solution and subsequent examination via TEM (JEM-2100, JEOL, Japan).

NaCl, SDS, and urea can disaggregate intermolecular interaction. Hence, 0.1 mL of non-PEGylated PLA@R NPs were diluted with 1 mL of these chemical materials (500 mM) and the particle size were assessed immediately by Nano ZS Zetasizer instrument (Malvern, UK).

### 4.4 *In vitro* drug release

With PBS (pH 7.4) containing 30% (v/v) ethanol as the release medium, the release of RSL3 was investigated with light (100 mW/cm$^2$, 2 min) or in the dark. At different time points, 1 mL of dialysate was withdrawn to investigate the release behaviors of RSL3 using high performance liquid chromatography (HPLC).

### 4.5 Cell culture

A549 and LLC cells were cultured in DMEM supplemented with 10% (v/v) FBS and penicillin/streptomycin. All cells were maintained in a humidified atmosphere of 5% $CO_2$ at 37 °C. Cell culture dishes/plates, round coverslips, 20 mm glass-bottom dishes, and centrifuge tubes were obtained from NEST Biotechnology Co., Ltd. (Wuxi, China).

### 4.6 *In vitro* cell toxicity assay

The *in vitro* cytotoxicity of PLA@R NPs was assessed against A549 and LLC cells using the MTT assay. Briefly, cells were seeded at a density of 5000 cells/well in 96-well plates and cultured for 12 h before replacing the medium. Subsequently, the cells were incubated with different concentrations of the PLA NPs, Mix Sol and PLA@R NPs for 4 h. The cells were exposed light irradiation (660 nm, 100 mW/cm$^2$ for 2 min) or not and then incubated for another 44 h. Subsequently, 20 μL of MTT (5 mg/mL) solution was added and then incubated at 37 °C. After 4 h of incubation, the formazan crystals were dissolved in 200 μL of dimethyl sulfoxide (DMSO). Finally, the absorbance of samples was evaluated using Varioskan Flash multimode microreader.

### 4.7 Design and fabrication of the microfluidic chip

The chip features 3D structure channels, with each chip contains four channels (15 mm in length, 1.5 mm in width, and 0.5 mm in height). The fabrication of the chip was carried out using a method that has been previously reported [30].

### 4.8 Construction of TOC

A549 cells were collected and configured into a cell suspension at a density of 1 × 10$^6$ cells/mL. Then, 20 μL of the cell suspension was injected into upper channel of the chip and cultured overnight at 37 °C with 5% $CO_2$ for later use.

### 4.9 Cell uptake

Cellular uptake of drugs *in vitro* was examined using confocal microscopy. Initially, cells were seeded in a TOC of 4.8. Subsequently, the medium was changed to include Mix solution or PLA@R NPs (PpIX both at 2 μg/mL) at a flow rate of 10 μL/min or keep it static for 1 or 4 h. The uptake was stopped and washed for 3 times by 4 °C PBS and fixed with 4% formaldehyde. Then, Hoechst 33342 was applied to stain the cell nuclei. Finally, the confocal laser scanning microscopy (CLSM, TCS SP2/AOBS, LEICA, Germany) was used to visualize them. The images were processed using ImageJ software.

### 4.10 ROS and LPO assay

Cells were cultured dynamically (10 μL/min) with medium containing PBS, PLA@R NPs, Mix Sol, PLA@R NPs + Ferrostatin-1 or PLA@R NPs + VC for 4 h with or without light irradiation treatment (660 nm, 100 Mw/cm$^2$ for 2 min). The cells were rinsed with PBS for three times. Then the cells were incubated with 2,7-Dichlorodihydrofluorescein diacetate (DCFH-DA) (10 μM) for 20 min to determine ROS production. Or the cells were incubated with boron-dipyrromethene (BODIPY) (1 μM) for 20 min to determine LPO production. After that, the cells were rinsed again with PBS three times. Finally, ROS or LPO production was observed using a laser confocal scanning microscope and analyzed using ImageJ software.

### 4.11 Determination of GSH content

Cells were cultured dynamically (10 μL/min) with medium containing PBS, PLA@R NPs or Mix Sol for 4 h with or without light irradiation treatment (660 nm, 100 mW/cm$^2$ for 2 min). The cells were rinsed three times with PBS. Then, the cells were

collected by trypsinization and GSH, and oxidized glutathione (GSSG) content was determined using glutathione kits.

### 4.12 Construction and characterization of vascularized TOC

The chip was treated with a mixture of matrigel and serum-free medium at a ratio of 1:30, and then left in a parallel refrigerator at 4 °C overnight to cure. Prior to placing the cells in the chamber, the unbound residual matrix adhesive is eliminated through a culture wash. HUVECs were collected and configured into a cell suspension at a density of $1 \times 10^6$ cells/mL. Then, 20 μL of HUVECs suspension was injected into upper channel of the chip and cultured for 3 h at 37 °C with 5% $CO_2$. Another 20 μL cell suspension was injected and then the chip was inverted and incubated for another 3 h to make it stick to the wall. 20 μL of the A549 cell suspension (cell density of $1 \times 10^6$ cells/mL) was injected into the lower channel of the chip. The chip was incubated at 37 °C. The culture medium was changed every 24 h until the cells were overgrown. The barrier integrity of monolayer vessel was characterized using immunofluorescence staining. Briefly, HUVECs were fixed with 4% paraformaldehyde, permeabilized with 0.1% Triton X for 10 min, and blocked with 2% bovine serum albumin (BSA) reconstituted in 1× PBS for 1 h at room temperature. After that, cells were incubated with ZO-1 mAb for 1 h, followed by nucleus staining with Hoechst for 5 min. Fluorescence images were obtained using a confocal laser scanning microscope.

### 4.13 Permeability behavior of PLA@R NPs on vascularized TOC

The upper channel of the vascularized TOC was injected with either Mix Sol or PLA@R NPs at a rate of 10 μL/min, while the lower channel was filled with blank culture medium. The chip was incubated at 37 °C and 5% $CO_2$ for 4, 8 and 12 h, respectively, and the lower channel culture medium was collected. The fluorescence intensity of the samples was quantitatively measured by the microplate reader.

### 4.14 Antiproliferation effect of PLA@R NPs with vascularized TOC

The medium containing PBS, PLA@R NPs or Mix Sol were dynamically perfused into the chip upper channel and cultured at 37 °C and 5 % $CO_2$ for 24, 36, 48 and 72 h with or without light irradiation treatment (660 nm, 100 mW/cm$^2$ for 2 min). Ki67 monoclonal antibody (ABclonal Technology) and Ki67 ELISA Kit (mlBio) were used to investigate tumor cell proliferation on chip.

### 4.15 Animal studies

Sprague–Dawley rats (180–220 g) and C57BL/6 mice (18–22 g) were obtained from the Laboratory Animal Center of Shenyang Pharmaceutical University (Shenyang, Liaoning, China). All the animal experiments were performed according to the Guidelines for the Care and Use of Laboratory Animals approved by the Institutional Animal Ethical Care Committee (IAEC) of Shenyang Pharmaceutical University.

### 4.16 *In vivo* pharmacokinetic study

Sprague–Dawley male rats (weighing 200 to 220 g) were used to study the *in vivo* pharmacokinetic of PLA@R NPs. The rats were fasted for 12 h before the experiment and divided into 2 groups randomly: Mix Solution (Mix Sol) and PLA@R NPs at an equivalent dose of 2 mg/kg PpIX and RSL3 dose of 1 mg/kg. Formulations were injected into the tail vein. At 0.08, 0.25, 0.5, 1, 2, 4, 6, 8, 12 and 24 h after administration, 0.5 mL of blood was sampled into an ethylene diamine tetra-acetic acid (EDTA)-coated tube and centrifuged immediately to collect plasma. The plasma samples were extracted by protein precipitation with acetonitrile. The concentration of PLA was analyzed using Varioskan Flash multimode microreader.

### 4.17 *In vivo* biodistribution

The LLC cells ($1 \times 10^6$ cells) were subcutaneously implanted into the flanks of female C57BL/6 mice (body weight 20 g) respectively. Once the average tumor volume was approximately 300 mm$^3$, the mice were randomly divided into 2 groups. Subsequently, Mix Sol and PLA@R NPs were administered via tail vein injection at an equivalent PpIX dose of 2 mg/kg and RSL3 dose of 1 mg/kg to the mice. The mice were then euthanized at predetermined time points (4, 8, and 12 h) to collect heart, liver, spleen, lung, kidney, and tumor tissues. The fluorescence intensity of major tissues and tumors was assessed using an *in vivo* imaging system (IVIS) imaging system (PerkinElmer).

### 4.18 *In vivo* antitumor efficacy

The LLC cells ($1 \times 10^6$ cells) were implanted subcutaneously in the flanks of female C57BL/6 mice (body weight 20 g) respectively. When the tumor reached 100 mm$^3$, the mice were randomly divided into 6 groups: PBS, Mix Sol, Mix Sol + Light, PLA NPs + Light, PLA@R NPs, and PLA@R NPs+ Light. These formulations were administrated every other day for a total of 5 times at equivalent concentrations of PpIX (2 mg/kg) and RSL3 (1 mg/kg). Meanwhile, the tumor volume and body weight of mice were measured and recorded daily. The animals were sacrificed when the average tumor size reached 1200 mm$^3$ in the control group. At the end of the treatment, the mice were sacrificed and the blood was collected and centrifuged at 4000 rpm for 10 min to obtain the serum for hepatic and renal liver function (alanine aminotransferase (ALT) and aspartate aminotransferase (AST)) and kidney function (creatinine (CRE) and blood urea nitrogen (BUN)) analysis. The tumor samples were also stained with HIF-1$\alpha$. The tumor volume and burden were calculated as follows (Eqs. (1) and (2) ):

$$\text{Tumor volume } (\text{mm}^3) = (L \times W \times W)/2 \quad (1)$$

$$\text{Tumor burden } (\%) = (W_{\text{tumor}}/W_{\text{mouse}}) \times 100 \quad (2)$$

where $L$ is the longest length of the tumor, $W$ is the shortest width across the center of the tumor, $W_{\text{tumor}}$ is the weight of tumor, and $W_{\text{mouse}}$ is the weight of mouse.

### 4.19 Statistical analysis

Statistical comparison between groups was analyzed with Student's t test and one-way analysis of variance (ANOVA). All results of the statistical analysis were expressed as a mean ± standard deviation (SD).

**Electronic Supplementary Material**: Supplementary material (further details of the mass spectrum, $^1$H-NMR spectrum, HIF-1$\alpha$

measurements and hepatorenal function parameters measurements) is available in the online version of this article at https://doi.org/10.26599/NR.2025.94907374.

## Data availability

All data needed to support the conclusions in the paper are presented in the manuscript and/or the Electronic Supplementary Material. Additional data related to this paper may be requested from the corresponding author upon request.

## Acknowledgements

Funding was generously provided by the Project of China-Japan Joint International Laboratory of Advanced Drug Delivery System Research and Translation of Liaoning Province (No. 2024JH2/102100007), Basic research project of 2024 Liaoning Provincial Department of Education Program (No. LJ212410163045), Liaoning Provincial Department of Education Program (No. LJKMZ20221353), and the open fund of National Key Laboratory of Advanced Drug Formulations for Overcoming Delivery Barriers (No. 2024-KFB-003).

## Declaration of competing interest

The authors declare that they have no known competing financial interests or personal relationships that could have appeared to influence the work reported in this paper.

## Author contribution statement

C. T. T.: Data curation, project administration, validation, writing manuscript, experimental design,funding acquisition. W. J. M.: Project administration, validation, experimental design. J. B. S.: Project administration, validation, experimental design. J. D.: Data curation, validation. Z. P. G.: Project administration. H. W. T.: Validation. A. K.: Resources. K. T.: Resources. R. G. X.: Supervision. C. L.: Supervision. X. B. W.: Conceptualization, supervision, writing – review & editing, funding acquisition. K. K.: Conceptualization, supervision, writing – review & editing, funding acquisition. All the authors have approved the final manuscript.

## Informed consent

Not applicable.

## Ethics statement

All the animal experiments were performed according to the Guidelines for the Care and Use of Laboratory Animals approved by the Institutional Animal Ethical Care Committee of Shenyang Pharmaceutical University (Ethical code: SYPU-IACUC-2024-0311-066).

## Use of AI statement

None.

## References

[1] Li, Y. G.; Zhang, P.; Xie, Y. J.; Yang, J. P.; Yang, Y. Q.; Shi, L. L.; Wu, W. B.; Li, Z. Photosensitizers with multiple degradation modes for efficient and postoperatively safe photodynamic therapy. *Biomaterials* **2023**, *299*, 122182.

[2] Wu, W. T.; Shao, X. D.; Zhao, J. Z.; Wu, M. B. Controllable photodynamic therapy implemented by regulating singlet oxygen efficiency. *Adv. Sci. (Weinh.)* **2017**, *4*, 1700113.

[3] Secret, E.; Maynadier, M.; Gallud, A.; Chaix, A.; Bouffard, E.; Gary-Bobo, M.; Marcotte, N.; Mongin, O.; El Cheikh, K.; Hugues, V. et al. Two-photon excitation of porphyrin-functionalized porous silicon nanoparticles for photodynamic therapy. *Adv. Mater.* **2014**, *26*, 7643–7648.

[4] Shen, Y. Z.; Shuhendler, A. J.; Ye, D. J.; Xu, J. J.; Chen, H. Y. Two-photon excitation nanoparticles for photodynamic therapy. *Chem. Soc. Rev.* **2016**, *45*, 6725–6741.

[5] Fan, W. P.; Huang, P.; Chen, X. Y. Overcoming the Achilles' heel of photodynamic therapy. *Chem. Soc. Rev.* **2016**, *45*, 6488–6519.

[6] Yu, L.; Liu, Z.; Xu, W.; Jin, K.; Liu, J. L.; Zhu, X. H.; Zhang, Y.; Wu, Y. H. Towards overcoming obstacles of type II photodynamic therapy: Endogenous production of light, photosensitizer, and oxygen. *Acta Pharm. Sin. B* **2024**, *14*, 1111–1131.

[7] Meng, X.; Deng, J.; Liu, F.; Guo, T.; Liu, M. Y.; Dai, P. P.; Fan, A. P.; Wang, Z.; Zhao, Y. J. Triggered all-active metal organic framework: Ferroptosis machinery contributes to the apoptotic photodynamic antitumor therapy. *Nano Lett.* **2019**, *19*, 7866–7876.

[8] Zhang, L.; Fan, Y. D.; Yang, Z.; Yang, M.; Wong, C. Y. NIR-II-driven and glutathione depletion-enhanced hypoxia-irrelevant free radical nanogenerator for combined cancer therapy. *J. Nanobiotechnol.* **2021**, *19*, 265.

[9] Jiang, X. J.; Stockwell, B. R.; Conrad, M. Ferroptosis: Mechanisms, biology and role in disease. *Nat. Rev. Mol. Cell Biol.* **2021**, *22*, 266–282.

[10] Stockwell, B. R. Ferroptosis turns 10: Emerging mechanisms, physiological functions, and therapeutic applications. *Cell* **2022**, *185*, 2401–2421.

[11] Zhao, L.; Zhou, X. X.; Xie, F.; Zhang, L.; Yan, H. Y.; Huang, J.; Zhang, C.; Zhou, F. F.; Chen, J.; Zhang, L. Ferroptosis in cancer and cancer immunotherapy. *Cancer Commun. (Lond)* **2022**, *42*, 88–116.

[12] Jelinek, A.; Heyder, L.; Daude, M.; Plessner, M.; Krippner, S.; Grosse, R.; Diederich, W. E.; Culmsee, C. Mitochondrial rescue prevents glutathione peroxidase-dependent ferroptosis. *Free Radical Biol. Med.* **2018**, *117*, 45–57.

[13] Wu, J.; Feng, Z.; Chen, L.; Li, Y.; Bian, H. J.; Geng, J. J.; Zheng, Z. H.; Fu, X. H.; Pei, Z.; Qin, Y. F. et al. TNF antagonist sensitizes synovial fibroblasts to ferroptotic cell death in collagen-induced arthritis mouse models. *Nat. Commun.* **2022**, *13*, 676.

[14] Hangauer, M. J.; Viswanathan, V. S.; Ryan, M. J.; Bole, D.; Eaton, J. K.; Matov, A.; Galeas, J.; Dhruv, H. D.; Berens, M. E.; Schreiber, S. L. et al. Drug-tolerant persister cancer cells are vulnerable to GPX4 inhibition. *Nature* **2017**, *551*, 247–250.

[15] Yang, W. S.; SriRamaratnam, R.; Welsch, M. E.; Shimada, K.; Skouta, R.; Viswanathan, V. S.; Cheah, J. H.; Clemons, P. A.; Shamji, A. F.; Clish, C. B. et al. Regulation of ferroptotic cancer cell death by GPX4. *Cell* **2014**, *156*, 317–331.

[16] Shui, S. F.; Zhao, Z. L.; Wang, H.; Conrad, M.; Liu, G. Q. Non-enzymatic lipid peroxidation initiated by photodynamic therapy drives a distinct ferroptosis-like cell death pathway. *Redox Biol.* **2021**, *45*, 102056.

[17] Wang, H. Y.; Qiao, C.; Guan, Q. T.; Wei, M. J.; Li, Z. H. Nanoparticle-mediated synergistic anticancer effect of ferroptosis and photodynamic therapy: Novel insights and perspectives. *Asian J. Pharm. Sci.* **2023**, *18*, 100829.

[18] Zhu, T.; Shi, L. L.; Yu, C. Y.; Dong, Y. B.; Qiu, F.; Shen, L. Y.; Qian, Q. H.; Zhou, G. Y.; Zhu, X. Y. Ferroptosis promotes photodynamic therapy: Supramolecular photosensitizer-inducer nanodrug for enhanced cancer treatment. *Theranostics* **2019**, *9*, 3293–3307.

[19] da Silva, D. B.; da Silva, C. L.; Davanzo, N. N.; da Silva Souza, R.; Correa, R. J.; Tedesco, A. C.; Riemma Pierre, M. B. Protoporphyrin IX (PpIX) loaded PLGA nanoparticles for topical Photodynamic Therapy of melanoma cells. *Photodiagnosis Photodyn. Ther.* **2021**, *35*, 102317.

[20] Piao, Y.; Himbert, S.; Li, Z. F.; Liu, J.; Zhao, Z. H.; Yu, H. H.; Liu, S. S.; Shao, S. Q.; Fefer, M.; Rheinstädter, M. C. et al. Alkylated EDTA potentiates antibacterial photodynamic activity of protoporphyrin. *J. Nanobiotechnol.* **2024**, *22*, 161.

[21] Song, R. D.; Li, T. L.; Ye, J. Y.; Sun, F.; Hou, B.; Saeed, M.; Gao, J.; Wang, Y. J.; Zhu, Q. W.; Xu, Z. A. et al. Acidity-Activatable dynamic nanoparticles boosting ferroptotic cell death for immunotherapy of cancer. *Adv. Mater.* **2021**, *33*, 2101155.

[22] Wang, C. C.; Wang, J.; Pan, X.; Yu, S.; Chen, M. Q.; Gao, Y.; Song, Z. L.; Hu, H. Y.; Zhao, X. L.; Chen, D. W. et al. Reversing ferroptosis resistance by MOFs through regulation intracellular redox homeostasis. *Asian J. Pharm. Sci.* **2023**, *18*, 100770.

[23] Fu, S. W.; Li, G. T.; Zang, W. L.; Zhou, X. Y.; Shi, K. X.; Zhai, Y. L. Pure drug nano-assemblies: A facile carrier-free nanoplatform for efficient cancer therapy. *Acta Pharm. Sin. B* **2022**, *12*, 92–106.

[24] Zhang, C. Z.; Zuo, Y.; Zhang, T. T.; Zhang, X.; Ling, J.; Liu, C. Q.; Chen, H. Y.; Zhou, X.; Wang, M. L.; Deng, Y. et al. Advances in nanoscale carrier-based approaches to reduce toxicity and enhance efficacy of podophyllotoxin. *Acta Mater. Med.* **2023**, *2*, 430–448.

[25] Li, G. T.; Sun, B. J.; Li, Y. Q.; Luo, C.; He, Z. G.; Sun, J. Small-Molecule prodrug nanoassemblies: An emerging nanoplatform for anticancer drug delivery. *Small* **2021**, *17*, 2101460.

[26] Li, G. T.; Jin, Q. H.; Xia, F. L.; Fu, S. W.; Zhang, X. B.; Xiao, H. Y.; Tian, C. T.; Lv, Q. Z.; Sun, J.; He, Z. G. et al. Smart stimuli-responsive carrier-free nanoassembly of SN38 prodrug As efficient chemotherapeutic nanomedicine. *Acta Mater. Med.* **2023**, *2*, 54–63.

[27] Kusznir, E. A.; Hau, J. C.; Portmann, M.; Reinhart, A. G.; Falivene, F.; Bastien, J.; Worm, J.; Ross, A.; Lauer, M.; Ringler, P. et al. Propensities of fatty acid-modified ASOs: Self-Assembly vs albumin binding. *Bioconjug. Chem.* **2023**, *34*, 866–879.

[28] Frenette, M.; Scaiano, J. C. Evidence for hydroxyl radical generation during lipid (linoleate) peroxidation. *J. Am. Chem. Soc.* **2008**, *130*, 9634–9635.

[29] Tian, C. T.; Zheng, S. Z.; Liu, X. Y.; Kamei, K. I. Tumor-on-a-chip model for advancement of anti-cancer nano drug delivery system. *J. Nanobiotechnol.* **2022**, *20*, 338.

[30] Zhuang, J. L.; Zhang, J.; Wu, M. H.; Zhang, Y. Q. A dynamic 3D tumor spheroid chip enables more accurate nanomedicine uptake evaluation. *Adv. Sci. (Weinh.)* **2019**, *6*, 1901462.

[31] Cho, E. C.; Zhang, Q.; Xia, Y. N. The effect of sedimentation and diffusion on cellular uptake of gold nanoparticles. *Nat. Nanotechnol.* **2011**, *6*, 385–391.

[32] Abdalkader, R.; Kamei, K. I. Multi-corneal barrier-on-a-chip to recapitulate eye blinking shear stress forces. *Lab Chip* **2020**, *20*, 1410–1417.

[33] Aragon-Sanabria, V.; Pohler, S. E.; Eswar, V. J.; Bierowski, M.; Gomez, E. W.; Dong, C. VE-Cadherin disassembly and cell contractility in the endothelium are necessary for barrier disruption induced by tumor cells. *Sci. Rep.* **2017**, *7*, 45835.

[34] Saha, B.; Mathur, T.; Handley, K. F.; Hu, W.; Afshar-Kharghan, V.; Sood, A. K.; Jain, A. OvCa-Chip microsystem recreates vascular endothelium-mediated platelet extravasation in ovarian cancer. *Blood Adv.* **2020**, *4*, 3329–3342.